

Metadata of the article that will be visualized in OnlineFirst

ArticleTitle	The 2022 Goesan earthquake of the moment magnitude 3.8 along the buried fault in the central Korean Peninsula	
<hr/>		
Article Sub-Title		
Article CopyRight	Springer Nature B.V. (This will be the copyright line in the final PDF)	
Journal Name	Journal of Seismology	
<hr/>		
Corresponding Author	FamilyName Particle Given Name Suffix Division Organization Address Phone Fax Email URL ORCID	Son Minkyung Earthquake Research Center Korea Institute of Geoscience and Mineral Resources 124 Gwahak-ro, Yuseong-gu, Daejeon, 34132, Republic of Korea kersti@kigam.re.kr http://orcid.org/0000-0003-4862-8510
<hr/>		
Author	FamilyName Particle Given Name Suffix Division Organization Address Phone Fax Email URL ORCID	Lim Hobin Earthquake Research Center Korea Institute of Geoscience and Mineral Resources 124 Gwahak-ro, Yuseong-gu, Daejeon, 34132, Republic of Korea HBL@kigam.re.kr http://orcid.org/0000-0001-7510-4507
<hr/>		
Author	FamilyName Particle Given Name Suffix Division Organization Address Phone Fax Email URL ORCID	Cho Chang Soo Earthquake Research Center Korea Institute of Geoscience and Mineral Resources 124 Gwahak-ro, Yuseong-gu, Daejeon, 34132, Republic of Korea nemex@kigam.re.kr http://orcid.org/0000-0003-1404-0583
<hr/>		
Schedule	Received Revised Accepted	18 Oct 2023 22 Feb 2024
<hr/>		
Abstract	On October 28, 2022, a moment magnitude (Mw) 3.8 earthquake occurred in Goesan, South Korea,	

typically characterized as a stable continental region. Herein, we analyze 42 earthquakes, including the Mw 3.8 earthquake, the largest foreshock (Mw 3.3), which preceded the mainshock by 17 s, and the largest aftershock (Mw 2.9). The primary aim of this study is to identify interactions among the seismic events. To this end, we utilized the permanent seismic networks with the closest station at 8.3 km from the epicenter, and the temporary network deployed eight hours after the mainshock's occurrence. Relocation results delineate that the mainshock occurred at the southeastern tip of the hypocenter distribution of three foreshocks, trending west-northwest–east-southeast. The aftershocks form an overall spatially diffused seismic pattern that propagates toward both ends of the inferred lineament in the downdip direction. The rupture directivity of the mainshock, along with waveform similarity across the mainshock and foreshocks, confirms the inferred geometry, corresponding well with the focal mechanisms of the mainshock and the largest foreshock. We demonstrate that the change in Coulomb failure stress (Δ CFS) by the largest foreshock was positive where the mainshock occurred and that the mainshock generated Δ CFS capable of triggering the propagation of the aftershocks.

Keywords (separated by '-') Stable continental region - Earthquake interaction - Coulomb failure stress - Waveform similarity - Foreshock - Aftershock

Footnote Information • The 2022 Goesan earthquake (Mw 3.8) was preceded by the Mw 3.3 event in ~17s. • This study determined how one seismic event influenced the next event in stable continental regions. • The Mw 3.3 foreshock generated enough stress to trigger the mainshock along the buried fault. The online version contains supplementary material available at <https://doi.org/10.1007/s10950-024-10201-y>.



2 The 2022 Goesan earthquake of the moment magnitude 3.8 3 along the buried fault in the central Korean Peninsula

4 Hobin Lim^{ID} · Chang Soo Cho^{ID} ·
5 Minkyung Son^{ID}

6 Received: 18 October 2023 / Accepted: 22 February 2024
7 © Springer Nature B.V. 2024

AQ1 Abstract On October 28, 2022, a moment magnitude (Mw) 3.8 earthquake occurred in Goesan, South Korea, typically characterized as a stable continental region. Herein, we analyze 42 earthquakes, including the Mw 3.8 earthquake, the largest foreshock (Mw 3.3), which preceded the mainshock by 17 s, and the largest aftershock (Mw 2.9). The primary aim of this study is to identify interactions among the seismic events. To this end, we utilized the permanent seismic networks with the closest station at 8.3 km from the epicenter, and the temporary network deployed eight hours after the mainshock's occurrence. Relocation

results delineate that the mainshock occurred at the southeastern tip of the hypocenter distribution of three foreshocks, trending west-northwest–east-southeast. The aftershocks form an overall spatially diffused seismic pattern that propagates toward both ends of the inferred lineament in the downdip direction. The rupture directivity of the mainshock, along with waveform similarity across the mainshock and foreshocks, confirms the inferred geometry, corresponding well with the focal mechanisms of the mainshock and the largest foreshock. We demonstrate that the change in Coulomb failure stress (Δ CFS) by the largest foreshock was positive where the mainshock occurred and that the mainshock generated Δ CFS capable of triggering the propagation of the aftershocks.

Keywords Stable continental region · Earthquake interaction · Coulomb failure stress · Waveform similarity · Foreshock · Aftershock

1 Introduction

On October 28, 2022, at 23:27:50 UTC, a moment magnitude (Mw) 3.8 earthquake occurred in the town of Goesan in the central region of South Korea (Fig. 1); there have been no reports of casualties or significant damage caused by the mainshock. The Korea Meteorological Administration (KMA) reported its local magnitude as 4.1. This region had

A1 **Highlights** • The 2022 Goesan earthquake (Mw 3.8)
A2 was preceded by the Mw 3.3 event in ~17 s.
A3 • This study determined how one seismic event influenced
A4 the next event in stable continental regions.
A5 • The Mw 3.3 foreshock generated enough stress to trigger
A6 the mainshock along the buried fault.

A7 **Supplementary Information** The online version
A8 contains supplementary material available at <https://doi.org/10.1007/s10950-024-10201-y>.

A10 H. Lim · C. S. Cho · M. Son (✉)
A11 Earthquake Research Center, Korea Institute of Geoscience
A12 and Mineral Resources, 124 Gwahak-ro, Yuseong-gu,
A13 Daejeon 34132, Republic of Korea
A14 e-mail: kersti@kigam.re.kr

A15 H. Lim
A16 e-mail: HBL@kigam.re.kr

A17 C. S. Cho
A18 e-mail: nemex@kigam.re.kr

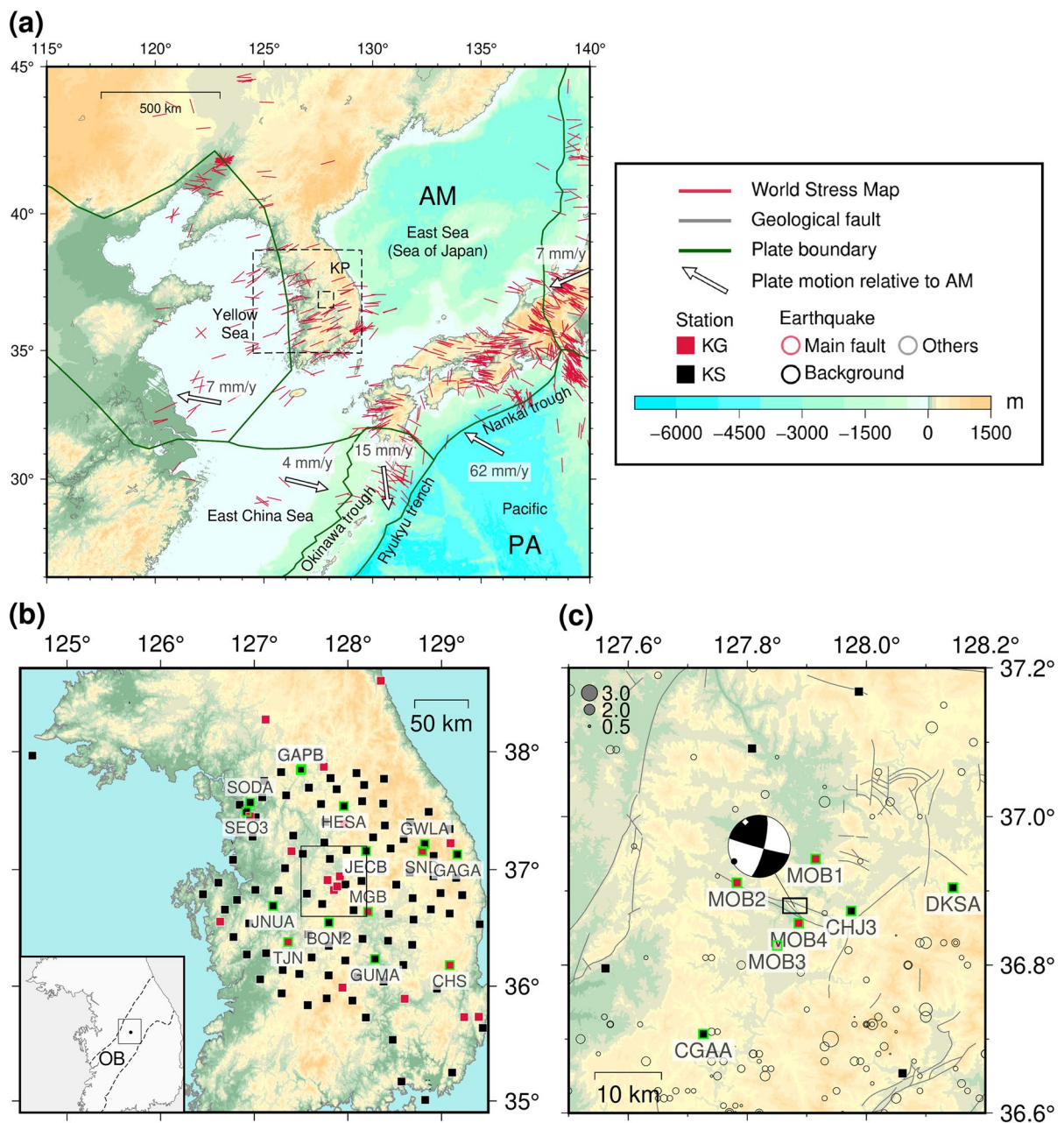


Fig. 1 Distribution of the Goesan earthquakes and tectonic setting. **a** Maximum horizontal crustal stress with the tectonic setting around the Korean Peninsula. Stress is obtained from the World Stress Map (Heidbach et al. 2018). Plate boundary is from Bird (2003). Larger and smaller dashed boxes indicate regions of **(b)** and **(c)**, respectively. **b** Stations used in this study. Inset shows the geological province, Okcheon Belt (OB), including the epicenters. The box indicates the region of **(c)**. **c** Magnified map including the stations used to determine

hypocenters. The box indicates the region of the map view in Fig. 5a. The background seismicity in 1978–2022 is plotted (seismicity from '<https://necis.kma.go.kr>' accessed on 31 July 2023). The geological faults are from '<https://doi.org/10.22747/data.20230712.5013>' (accessed on 2 May 2023). AM: Amurian Plate. PA: Pacific Plate. JF: Jogok Fault (Park 2005). KG: Korea Institute of Geoscience and Mineral Resources. KS: Korea Meteorological Administration. KP: Korean Peninsula

47 no reported destructive earthquakes since 1978, when
 48 modern seismic monitoring was initiated.

49 The Korean Peninsula is located in stable con-
 50 tinental regions with a relatively uniform ambient
 51 stress field in South Korea (Fig. 1a). The direction of
 52 the maximum horizontal compressional stress axis in
 53 inland South Korea is east-northeast–west-southwest
 54 (Fig. 1a). The region of the epicenter was within the
 55 Okcheon Belt, a geological province in South Korea,
 56 approximately 1,000 km from the closest Nankai
 57 Trough in Japan (Fig. 1a and b).

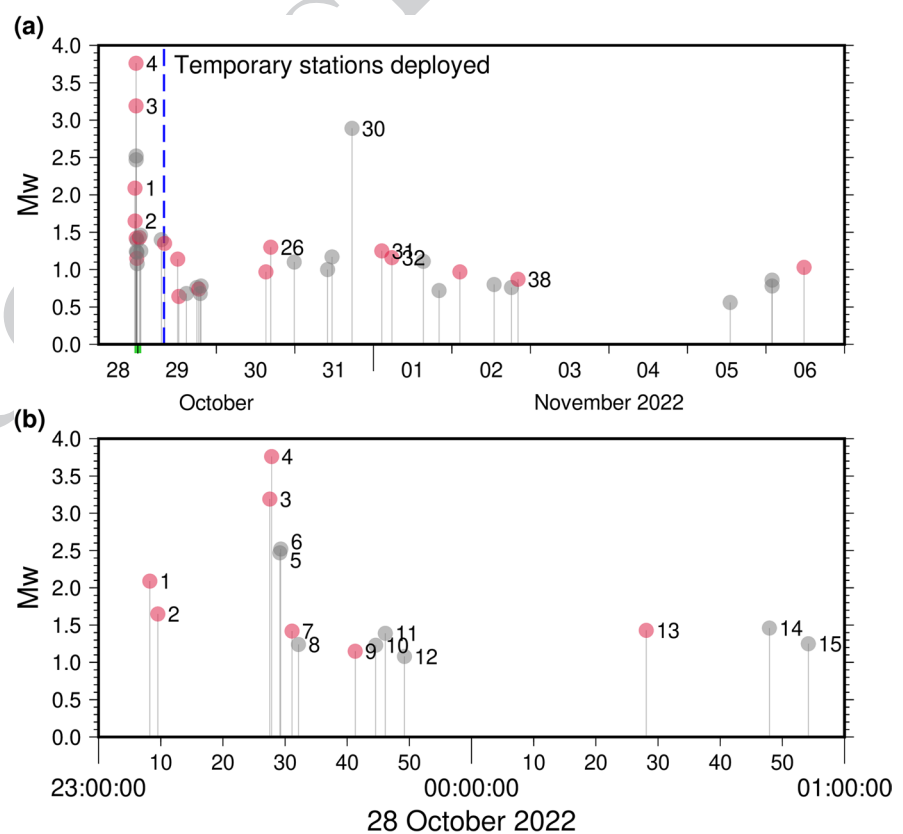
58 Geological faults, including the Jogok Fault (JF),
 59 are located in the region (Fig. 1c). The JF is subparallel
 60 to the strike of the mainshock’s nodal plane, with
 61 a maximum deviation of 10° (Fig. 1c). The main
 62 sense of slip across the JF is left-lateral (Park 2005),
 63 which is consistent with the focal mechanism of the
 64 mainshock (Fig. 1c). However, the lack of seismicity
 65 between the surface and subsurface at a focal depth
 66 of ~ 10 km limits further analysis.

67 Notably, the mainshock was preceded by a Mw
 68 3.3 foreshock that occurred at 23:27:33 on October

28, 2022 (UTC), approximately 17 s before the main-
 shock (events 3 and 4 in Fig. 2). Permanent stations
 recorded the largest foreshock’s S-wave coda interfer-
 ing with the P wave of the mainshock from a distance
 greater than ~ 135 km (Fig. 3). The Korea Institute
 of Geoscience and Mineral Resources deployed four
 temporary broadband stations within 10 km from
 the epicenter of the Mw 3.8 mainshock (see Fig. 1c).
 These stations began operation at 8:00:00 on October
 29, 2022 (UTC), approximately eight hours after the
 mainshock occurred (see the dashed line in Fig. 2a)
 and recorded the largest aftershock of Mw 2.9 (event
 30 in Fig. 2a).

This study utilized data from both the temporary
 and permanent stations to enhance constraints for
 locating hypocenters, complementing previous studies
 on the Goesan earthquakes (Hong et al. 2023; Kim
 et al. 2023; Sheen et al. 2023). We delved into pos-
 sible interactions among the foreshock, mainshock,
 and aftershocks, precisely relocating hypocenters and
 examining whether a coseismic static stress model
 can account for the associated successive seismicity.

Fig. 2 Chronology of the earthquake sequence.
a Period from October 28, 2022 to November 6, 2022. Red and grey circles represent events included in the main fault and others, respectively. A dashed line indicates the time when four temporary stations were deployed. **b** A magnified plot for a two-hour window, including events 1–15, as marked with a green tick on the time axis of (a)



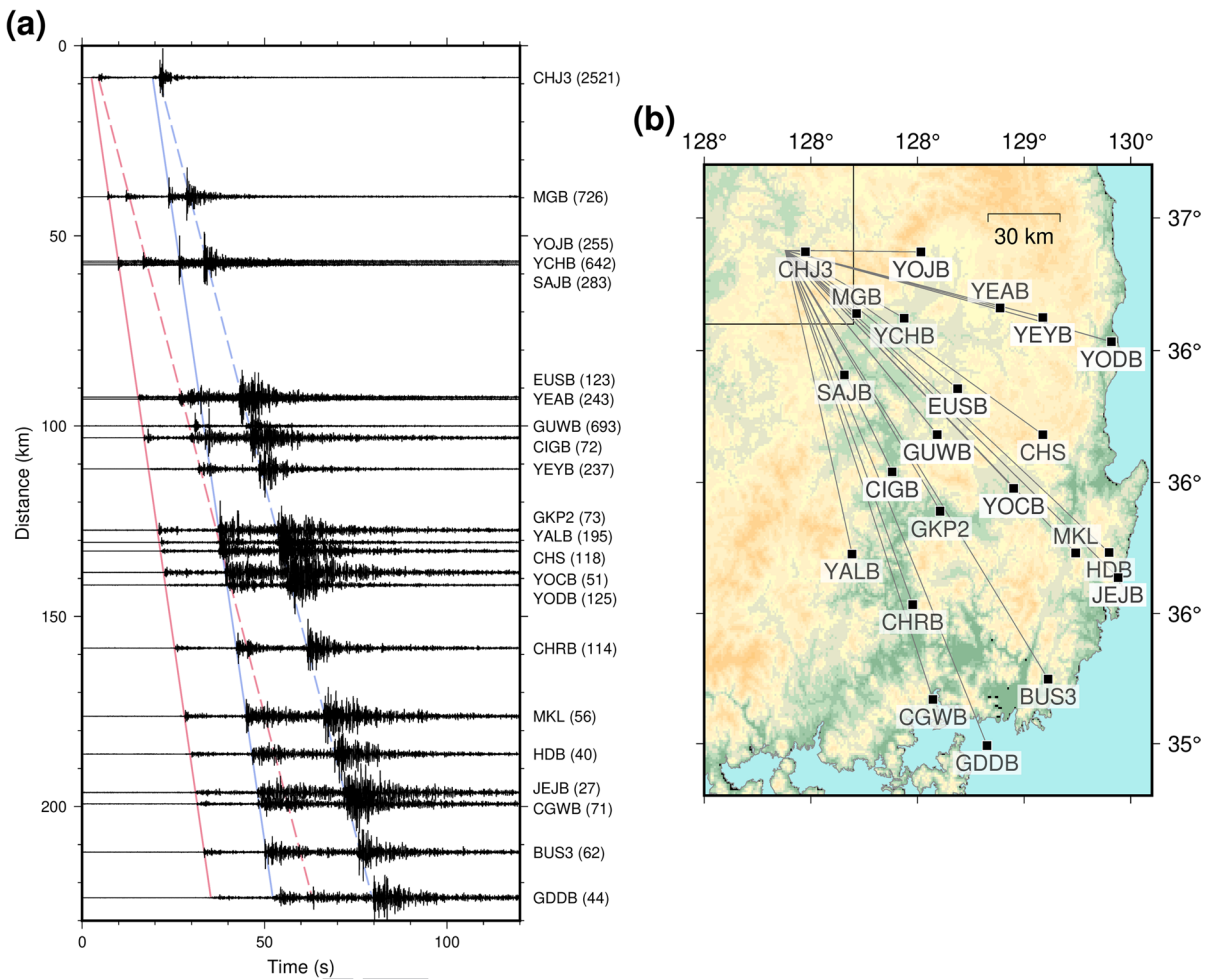


Fig. 3 Interference between the Mw 3.3 foreshock (event 3) and Mw 3.8 mainshock (event 4). **a** Vertical record sections of event 3 and event 4. Their difference in origin time is 17 s (Table 1). The trace is filtered in 2–8 Hz by acausal Butterworth of four poles. P and S wave arrivals are guided by solid and dashed lines, respectively. Faint red and blue lines are

events 3 and 4, respectively. The S waves of event 3 and the P waves of event 4 cross at ~ 135 km. The amplitude of the trace is normalized. Names of the stations are on the right, and the peak-to-peak amplitudes in $\mu\text{m/s}$ are within parentheses. The azimuth of the stations ranges from 90° to 170°. **b** Map of the station used in (a). A box in (b) indicates the region of Fig. 1c

November 10, 2022, vertical components of seismic waveforms were band-pass filtered at 2–14 Hz for time window durations of -1 s to 3 s in terms of P wave at three stations, CHJ3, DKSA, and CGAA (Fig. 1c). We used waveforms with a mean correlation coefficient greater than 0.3.

Subsequently, P and S wave arrival times in the vertical and transverse components, respectively, were measured manually at 11 stations including the four temporary stations (Fig. 1c), to enhance relocation accuracy and decrease the minimum magnitude of locatable events. Manual measurement was

99
100
101
102
103
104
105
106
107
108
109
110

91 This effort could contribute to a better understanding
92 of earthquake triggering and interaction in stable con-
93 tinental regions.

94 2 Data and methods

95 2.1 Earthquake detection and relocation

96 We detected small-magnitude earthquakes using the
97 template-matching method based on the list of 30
98 events provided by the KMA. From October 28 to

111 employed to prevent cyclic-skipping and undesirable
 112 effects resulting from varying durations (Bachura and
 113 Fischer 2019). The initial hypocenters were deter-
 114 mined using *bayesloc* (Myers et al. 2007) with a 1-D
 115 velocity model for the Korean Peninsula based on
 116 the model described by Kim et al. (2022) originating
 117 from Kim and Kim (1983) (Table S1).

118 The double-difference method was applied to
 119 enhance the relative hypocenters based on the two
 120 sets of differential times (DT) for the P and S waves
 121 (Waldhauser and Ellsworth 2000). The first set com-
 122 prised differential travel times of event pairs from P
 123 and S arrival picks (DT_1) while the second set was
 124 based on waveform cross-correlation (DT_2) after the
 125 waveform was interpolated to 1,000 samples per sec-
 126 ond. In the waveform cross-correlation, we used a
 127 short window from -0.015 s to 0.015 s in terms of P
 128 or S arrival picked manually. We only used the DT_2 if
 129 $|DT_2 - DT_1| < 0.01$ s to prevent cyclic-skipping and
 130 unintended effects caused by various durations. The
 131 1,921 DT_1 helped to determine the overall distribu-
 132 tion of the relative hypocenters; the 1,591 DT_2 fine-
 133 tuned the hypocenters.

134 Finally, the hypocenters were shifted by the abso-
 135 lute hypocenter of the largest aftershock (event 30),
 136 presumed to have the highest accuracy as it was
 137 recorded by the temporary stations. We estimated
 138 the uncertainty of the relative hypocenters through
 139 a bootstrapping approach. A total of 370 pairs were
 140 considered (Fig. S1 in the supplementary materials),
 141 with 70% (i.e., 259 pairs) randomly selected without
 142 duplication. The perturbed relocated hypocenters
 143 were shifted by the unperturbed absolute hypocenter
 144 of event 30, and this process was repeated 1,000
 145 times.

146 2.2 Source spectrum fitting

147 We estimated the moment magnitude (Mw) and
 148 corner frequency (f_C) of earthquakes by fitting the
 149 S wave source spectrum with the Brune model
 150 (Brune 1970, 1971). The geometrical spreading
 151 and intrinsic attenuation were corrected to displace-
 152 ment source spectra, and the best-fitting model for
 153 the spectra was determined through a grid-search-
 154 ing scheme with an adopted range of domains and
 155 spacing (see details in Text S1 in the supplementary
 156 materials). The searching domain was set near the

initial values of Mw and f_C with the Snoker method
 157 (Snoker 1987; see details in Supplementary Text
 158 S2).

159 For the mainshock (event 4), we used data from
 160 8 stations in distance of 116–325 km (see the list
 161 of stations in Table S2 in the supplementary materi-
 162 als). For the largest aftershock (event 30), we used
 163 more stations, up to 17, in distance of 39–397 km,
 164 because it was free from coda interferences caused
 165 by preceding large-sized events. However, for the
 166 largest foreshock (event 3), we had no other choice
 167 but to use the closest single station, CHJ3, at a dis-
 168 tance of 8 km, due to the S coda interfering with
 169 the P wave of the mainshock (Fig. 3). This single
 170 measurement limited the reliability of the estimated
 171 f_C for event 3.

172 We employed the single-station approach using
 173 CHJ3 to estimate moment magnitudes for 40 earth-
 174 quakes, which were events 1 to 3, 5 to 29, and 31 to
 175 42. However, for event 30, we utilized 17 stations
 176 owing to the large amplitudes of the event, making it
 177 the largest aftershock.

2.3 Focal mechanism determination

179 We utilized the Time Domain Moment Tensor inver-
 180 sion tool (TDMT) (Dreger 2003; Minson and Dreger
 181 2008) to derive moment tensor solutions for the Mw
 182 3.8 mainshock (event 4) and Mw 3.3 foreshock (event
 183 3), based on the velocity model of Kim et al. (2011)
 184 (Fig. S2 in the supplementary materials). However,
 185 for the foreshock (event 3), we only applied data
 186 from three stations (CHS, SND, and TJN) within
 187 limited time windows because the S wave of the
 188 foreshock and P wave of the mainshock interfered at
 189 distances > 135 km (see Fig. 3). For the mainshock
 190 (event 4), we applied data from 11 stations spanning
 191 a distance of 72–306 km. The applied passbands for
 192 the mainshock and foreshock were 0.04–0.10 Hz
 193 and 0.09–0.20 Hz, respectively. The passband for
 194 the mainshock was tuned by trial and error to mini-
 195 mize the interference effect of coda from the largest
 196 foreshocks. The centroid depth was assessed every
 197 1 km between 1 and 17 km. (Fig. S2 in the supple-
 198 mentary materials). The focal mechanism of events 3
 199 and 30 were determined based on P wave polarity in
 200 the vertical component, using *focmec* (Snoker 2003)
 201 (Fig. S3).

203 2.4 Rupture directivity estimation

204 We used unilateral and bilateral rupture models to
 205 assess an azimuthal dependency of f_C . The reciprocal
 206 of the f_C is the apparent source duration Δt (Brune
 207 1970, 1971). In the unilateral model, the rupture
 208 propagated toward only one side laterally. In the bilat-
 209 eral model, the rupture propagated toward both sides
 210 with equal length and rupture velocity. The appar-
 211 ent source duration, Δt , can be modeled using Eqs.
 212 (1) and (2) for the unilateral and bilateral ruptures,
 213 respectively (Cesca et al. 2011).

$$214 \quad \Delta t(AZ) = -A\cos(AZ - STK) + B \quad (1)$$

$$216 \quad \Delta t(AZ) = A|\cos(AZ - STK)| + B \quad (2)$$

218 The AZ and STK stand for the azimuth to a sta-
 219 tion and the strike of the fault, respectively. The AZ
 220 is determined from the locations of the event and the
 221 station. Equations (1) and (2) assume that the fault
 222 has a lateral rupture direction with no vertical compo-
 223 nent. The A describes the fault's lateral width, L , with
 224 the relation $A = L/\beta$, where β represents the shear
 225 wave velocity (Cesca et al. 2011). Similarly, the B is
 226 defined as $B = t_r + L/V_R$, where t_r is the rise time,
 227 and V_R is the rupture velocity.

228 More general setups for rupture directivity, such as
 229 asymmetric bilateral rupture or involving the vertical
 230 component of the rupture direction, can be found in
 231 Cesca et al. (2011) and Park and Ishii (2015). How-
 232 ever, we applied Eqs. (1) and (2) to our analysis,
 233 simplifying the fault rupture to consist solely of lat-
 234 eral directions. We aimed to determine the positive
 235 unknowns A and B through least-square linear inver-
 236 sion, using the four possible STK values. These val-
 237 ues include opposing directions of a nodal plane. If
 238 either A or B becomes negative, we attempted another
 239 value for the STK .

240 2.5 Evaluation of change in the Coulomb failure
 241 stress

242 We also evaluated whether the changes in coseismic
 243 static stress of one earthquake induce subsequent
 244 earthquakes based on the concept of the change in
 245 the Coulomb Failure Stress (ΔCFS) (Lin and Stein

204; Ree et al. 2021; Kim et al. 2022). A positive
 246 ΔCFS indicates that the stress change causes
 247 the following event to have the assumed strike, dip,
 248 and rake. Conversely, a negative ΔCFS means that
 249 the stress change prevents the following event from
 250 occurring. The region with the negative ΔCFS is
 251 typically called the “stress shadow” (Freed 2005).
 252 We calculated the second-order tensor stress fields
 253 changed by the Mw 3.3 foreshock (event 3) and the
 254 Mw 3.8 mainshock (event 4) using the *Coulomb 3*
 255 program (Lin and Stein 2004).

256 For the mainshock (event 4), we assigned the
 257 “source fault” mechanism with the strike, dip, and
 258 rake values of 105° , 87° , and 13° , respectively
 259 (listed in Table 2), obtained from moment tensor
 260 inversion. These parameters were also applied to
 261 the source fault for the largest foreshock (event 3),
 262 instead of employing its own moment tensor solu-
 263 tion. The moment tensor inversion for event 30
 264 employed only three stations (TJN, SND, and CHS)
 265 and consequently provided a solution with low vari-
 266 ance reduction (54.8%) and a relatively high non-
 267 double-couple component (34%) (see the solution
 268 shown in Fig. S2).

269 The fault size was simplified as a square with
 270 widths of 0.18 km for event 3 (Mw 3.3) and 0.35 km
 271 for event 4 (Mw 3.8). The latter was based on f_C
 272 estimated in the source spectrum fitting. The f_C can
 273 be converted to the radius r_0 of a circular rupture
 274 model using $0.21\beta/f_C$, where β is the shear wave
 275 velocity (Madariaga 1976). We set β as 3.5 km/s.
 276 The size of square was determined to match the area
 277 of the corresponding circle. Changing the shape of
 278 rupture model was intended to simplify the calcula-
 279 tion of *Coulomb 3*, which does not carry a physi-
 280 cal meaning to make a change in interpretation. For
 281 event 3, as we were unable to obtain a reasonable
 282 f_C , the rupture area (r_0 of 0.1 km) was derived from
 283 the assumption that the earthquake has a stress drop
 284 of 30 MPa. This value is equal to the rounded-off
 285 stress drop of event 4 determined using its f_C .

286 The final procedure involved conversion from
 287 a stress tensor to a scalar, ΔCFS , in terms of the
 288 targeted focal mechanism defined by strike, dip,
 289 and rake, designated the “receiver fault.” We
 290 set Young’s modulus, Poisson ratio, and effec-
 291 tive frictional coefficient as 80 GPa, 0.25, and 0.4,
 292 respectively.

294 **3 Results**295 **3.1 Moment magnitude**

296 We denote moment magnitudes that were estimated
 297 through the source spectrum fitting as Mw^B ('B'
 298 stands for Brune) and those estimated through the
 299 TDMT inversion as Mw^{TDMT} . The 42 earthquakes
 300 have Mw^B ranging from 0.6 to 3.8 (Table 1). The
 301 Mw^B of the mainshock (event 4) was same as the
 302 Mw^{TDMT} of it (Mw 3.8). The Mw^B and Mw^{TDMT}
 303 of the largest foreshock (event 3) had a slight dif-
 304 ference by 0.1. (Mw^B 3.2 in Table 1; Mw^{TDMT} 3.3
 305 in Table 2). We preferred the Mw^{TDMT} for event 3
 306 because it was constrained by a larger number of
 307 stations, that is 3, compared to the Mw^B , which
 308 was based on the single station (CHJ3). The Mw^B
 309 of the largest aftershock (event 30) was 2.9. See
 310 Fig. S2 in the supplementary materials for the
 311 detailed results of the TDMT inversion for events
 312 3 and 4. Also, see Fig. S4–S6 in the supplementary
 313 materials for source spectrum fittings of events 3,
 314 4, and 30, respectively. The asymptotic value of the
 315 source spectrum model to 0 Hz directly refers to
 316 the seismic moment.

317 **3.2 Corner frequency (f_C) and directivity**

318 We observed azimuthal dependency in the recipro-
 319 cal of f_C across 8 stations for event 4 and 17 stations
 320 for event 30 (Fig. 4). The f_C is known to be affected
 321 by the directivity of rupture propagation. The f_C^{-1}
 322 of event 4 were distributed having the maximum at
 323 116° in azimuth (refer to station CHS for event 4 in
 324 Table S2; Fig. 4a). That is, the f_C^{-1} exhibited a single-
 325 lobe pattern in azimuth, implying a unilateral rupture
 326 that propagated toward the west-northwest (Fig. 4a).
 327 On the other hand, the f_C^{-1} of event 30 had two min-
 328 ima at 12° and 202° in azimuth (refer to stations KSA
 329 and BGD, respectively, in Table S2; Fig. 4b). The
 330 f_C^{-1} had a two-lobe pattern in azimuth with the two
 331 estimated maxima (Fig. 4b), which indicates that the
 332 rupture had elongated apparent durations toward both
 333 of the directions, the west-northwest–east-southeast.
 334 This describes a bilateral directivity along the fault
 335 strike. It is noteworthy that the estimated directiv-
 336 ity constrains the fault plane of the two nodal planes

derived from the focal mechanism, not depending on
 the spatial distribution of relocated hypocenters.

For event 4 (mainshock), the representative f_C was
 337 3.61 Hz, and for event 30, it was 9.0 Hz. These val-
 338 ues were obtained as the reciprocal of the constant
 339 term (B^{-1}) from the best-fitting sinusoidal curves in
 340 Fig. 4a and b, respectively. The r_0 of the mainshock,
 341 obtained from the representative f_C , was 0.20 km. The
 342 corresponding stress drop $\Delta\sigma$ was calculated with
 343 $\Delta\sigma = 7M_0/16r_0^3$, where M_0 is the seismic moment
 344 (Eshelby 1957). The $\Delta\sigma$ of the mainshock was
 345 29 MPa. Similarly, the r_0 and $\Delta\sigma$ of event 30 were
 346 0.08 km and 20 MPa, respectively.

347 **3.3 Fault attributable to the mainshock**

The focal mechanism solutions of the Mw 3.3 fore-
 351 shock (event 3) and Mw 3.8 mainshock (event 4)
 352 had coherent nodal planes, which are west-north-
 353 west–east-southeast vertical strike-slip faults with a
 354 dominant double-couple composition of the main-
 355 shock by 97% and the foreshock by 66% (Figs. 5a and
 356 S2; Table 2). Due to the small number of stations, we
 357 were unable to interpret the high non-double-couple
 358 composition of event 3 (Fig. S2 in the supplemen-
 359 tary materials). Relocated hypocenters of events 1,
 360 2, and 3 and the mainshock (event 4) constitute a
 361 plane with a horizontal direction that is consistent
 362 with the west-northwest–east-southeast nodal plane
 363 in the focal mechanisms of event 3 and the main-
 364 shock (Fig. 5a). Also, this nodal plane was consistent
 365 with the directivity observed in f_C to west-northwest
 366 (285° ; Fig. 4a). Lateral and vertical extension of this
 367 plane covered smaller events. All the events within
 368 this extended plane were labeled with 'm' stand-
 369 ing for 'main fault' in Table 1. They were marked
 370 as red color in Fig. 5 to distinguish the other events
 371 which were not included in the main fault. The west-
 372 northwest–east-southeast trend was also confirmed in
 373 previous studies (Hong et al. 2023; Kim et al. 2023;
 374 Sheen et al. 2023). Double-couple component of the
 375 focal mechanism for event 3 was similar to that con-
 376 strained with P wave polarity (Table 2).

377 Of the two nodal planes, the largest aftershock
 378 (event 30) could be attributed to a west-north-
 379 west–east-southeast plane. This plane is subparallel to
 380 the main fault (Figs. 5 and S6), and the rupture direc-
 381 tivity of event 30 (Fig. 4b) also aligns the fault plane
 382 trending west-northwest–east-southeast. The dip of

AQ2 **Table 1** List of the earthquakes

Event	Origin time (UTC)	Latitude (°)	Longitude (°)	Depth (km)	Mw ^B	f _C (Hz)
1 ^m	2022-10-28T23:08:14.8	36.87916	127.87828	13.28	2.1 ^a	-
2 ^m	2022-10-28T23:09:32.4	36.87954	127.87683	12.99	1.7 ^a	-
3 ^m	2022-10-28T23:27:33.5	36.87896	127.87705	13.00	3.2 ^a	(15.93) ^a
4 ^m	2022-10-28T23:27:50.2	36.87813	127.87979	12.83	3.8	3.61
5	2022-10-28T23:29:09.7	36.88351	127.86890	13.23	2.5 ^a	-
6	2022-10-28T23:29:18.8	36.88029	127.88341	12.78	2.5 ^a	-
7 ^m	2022-10-28T23:31:07.1	36.87890	127.87740	12.87	1.4 ^a	-
8	2022-10-28T23:32:09.3	36.88101	127.87781	12.58	1.2 ^a	-
9 ^m	2022-10-28T23:41:16.6	36.87797	127.88326	12.64	1.2 ^a	-
10	2022-10-28T23:44:35.0	36.87601	127.86418	11.44	1.2 ^a	-
11	2022-10-28T23:46:07.5	36.87983	127.87941	13.24	1.4 ^a	-
12	2022-10-28T23:49:12.4	36.88012	127.87857	13.17	1.1 ^a	-
13 ^m	2022-10-29T00:28:06.3	36.88001	127.87248	13.32	1.4 ^a	-
14	2022-10-29T00:47:55.2	36.87969	127.88278	13.29	1.5 ^a	-
15	2022-10-29T00:54:10.9	36.88313	127.87572	13.64	1.3 ^a	-
16	2022-10-29T07:09:43.1	36.88073	127.87794	13.01	1.4 ^a	-
17 ^m	2022-10-29T08:09:30.8	36.87801	127.88154	13.16	1.4 ^a	-
18 ^m	2022-10-29T12:10:55.9	36.87902	127.88057	13.21	1.1 ^a	-
19 ^m	2022-10-29T12:33:44.1	36.87782	127.88207	13.16	0.6 ^a	-
20	2022-10-29T14:50:38.2	36.88006	127.87935	13.68	0.7 ^a	-
21	2022-10-29T18:03:51.6	36.88250	127.88011	13.51	0.8 ^a	-
22 ^m	2022-10-29T18:38:23.3	36.87812	127.88221	13.22	0.7 ^a	-
23	2022-10-29T19:05:16.7	36.88099	127.88088	13.74	0.7 ^a	-
24	2022-10-29T19:21:00.2	36.88172	127.88150	13.50	0.8 ^a	-
25 ^m	2022-10-30T15:09:27.0	36.87701	127.88725	12.60	1.0 ^a	-
26 ^m	2022-10-30T16:37:59.6	36.87922	127.87793	12.93	1.3 ^a	-
27	2022-10-30T23:49:07.3	36.87942	127.88131	13.12	1.1 ^a	-
28	2022-10-31T10:00:23.7	36.87455	127.88148	13.09	1.0 ^a	-
29	2022-10-31T11:22:22.7	36.87994	127.88190	12.70	1.2 ^a	-
30	2022-10-31T17:27:52.8	36.88053	127.87695	12.89	2.9	9.0
31 ^m	2022-11-01T02:35:16.9	36.87775	127.88298	13.20	1.3 ^a	-
32 ^m	2022-11-01T05:40:34.7	36.87764	127.88171	13.14	1.2 ^a	-
33	2022-11-01T15:15:24.6	36.88009	127.88301	12.83	1.1 ^a	-
34	2022-11-01T20:03:57.6	36.87895	127.88365	12.74	0.7 ^a	-
35 ^m	2022-11-02T02:26:50.8	36.87759	127.88410	13.71	1.0 ^a	-
36	2022-11-02T12:55:19.1	36.87471	127.87609	13.54	0.8 ^a	-
37	2022-11-02T18:13:09.0	36.87941	127.88125	12.95	0.8 ^a	-
38 ^m	2022-11-02T20:12:33.3	36.87834	127.88223	13.16	0.9 ^a	-
39	2022-11-05T13:04:43.9	36.87661	127.88089	12.97	0.6 ^a	-
40	2022-11-06T01:51:57.8	36.88445	127.87680	11.72	0.9 ^a	-
41	2022-11-06T01:52:32.7	36.88041	127.87939	12.86	0.8 ^a	-
42 ^m	2022-11-06T11:39:25.8	36.87560	127.89049	13.39	1.0 ^a	-

Numbers are assigned in chronological order. Superscript m: event constituting the main fault; f_C: corner frequency estimated by the source spectrum fitting. a: measured with the single station with high uncertainty

the aftershock (68°) was slightly gentler than that of the mainshock (87°; Table 2). The P-axis of the faulting mechanisms observed in Fig. 5a was similar to

the direction of the maximum horizontal principal stress of the crust in South Korea suggested by Soh et al. (2018).

Table 2 Source properties of events 3, 4, and 30

Event	Mw ^{TDMT}	Strike (°)	Dip (°)	Rake (°)	Centroid depth	DC	CLVD
3	3.3	109; 18	84; 83	7; 174	14 km	66%	34%
3	-	104; 196	80; 81	-9; -170	-	-	-
4	3.8	105; 14	87; 77	13; 177	14 km	97%	3%
30	-	111; 208	68; 73	-19; -203	-	-	-

The preferred nodal plane is provided first for the strike, dip, and rake. Focal mechanisms for events 3 and 4 were determined using Time Domain Moment Tensor inversion (TDMT, Dreger 2003; Minson and Dreger 2008; the first and third rows). The focal mechanisms of events 3 and 30 were determined based on P wave polarity (Snoke 2003; the second and fourth rows). DC and CLVD indicate components of double couple component and compensated linear vector dipole, respectively

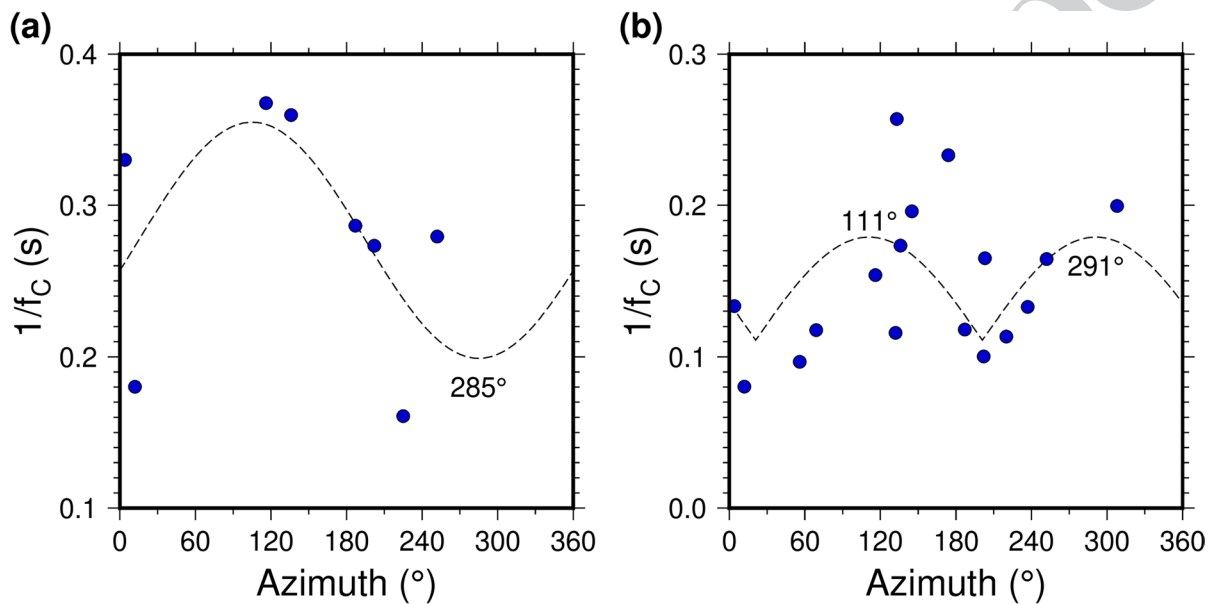


Fig. 4 Directivity of the mainshock and the largest aftershock. A reciprocal of f_C is plotted as a function of azimuth (AZ). **a** Mainshock (event 4) with unilateral rupture direction at 285° (west-northwest). **b** Largest aftershock (event 30) with bilateral rupture directions at 111° and 291° (west-northwest–east-southeast). The equations of the fitting

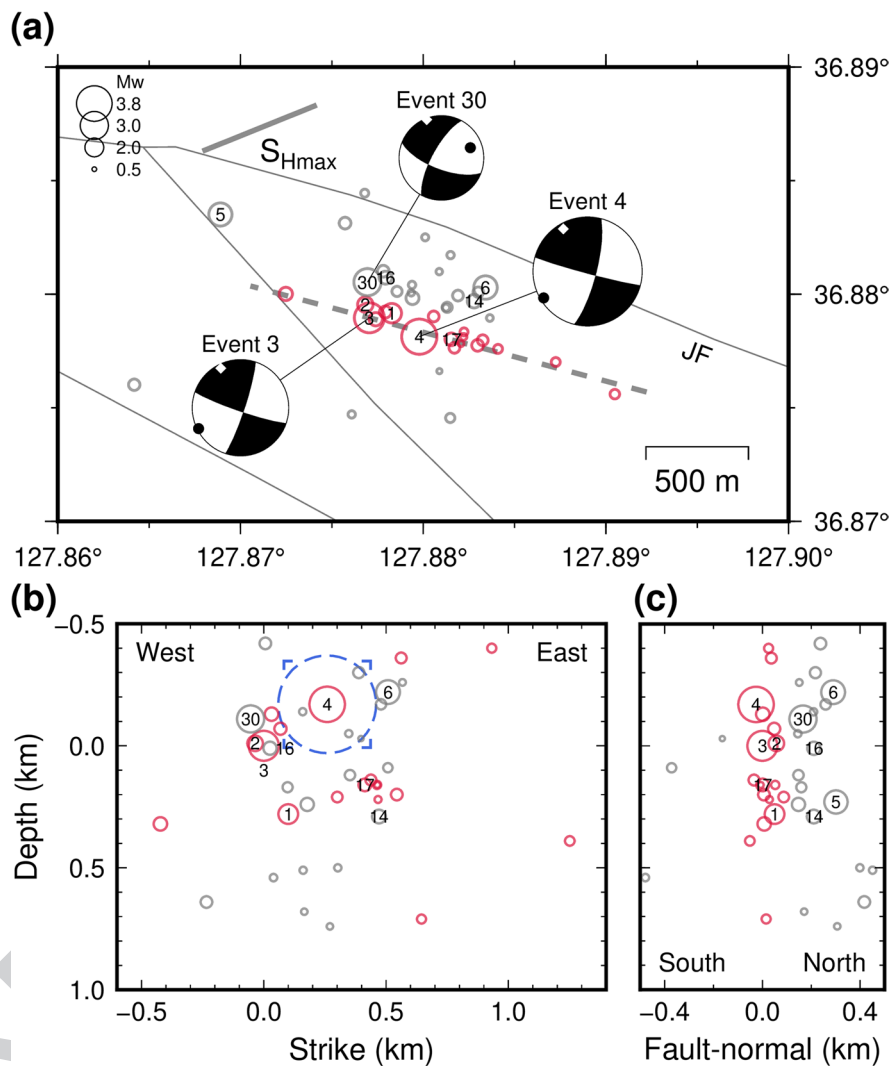
curves in (a) and (b) are $0.277 - 0.078\cos(AZ - 285^\circ)$ and $0.111 + 0.068|\cos(AZ - 111^\circ)|$, respectively. The equations were obtained with least-square linear regression with fixed azimuthal phases by 105° and 111° for event 4 and 30, respectively. The formulas for the curves representing rupture directivity were adopted from Cesca et al. (2011)

390 3.4 Changes in the Coulomb failure stress

391 We examined the spatiotemporal development of the
392 Goesan earthquakes in terms of the coseismic static
393 stress transfer using Δ CFSs. Figure 6 presents the
394 Δ CFSs for the Mw 3.3 foreshock (event 3) and Mw
395 3.8 mainshock (event 4). The Δ CFS of the mainshock
396 accumulated from the foreshock. The receiver fault
397 was set to the strike, dip, and rake of the mainshock
398 to assess the tendency for planar extension along the
399 “main fault.”

The general patterns in Δ CFS include the presence of four positive lobes in the horizontal slice at a depth of 12.8 km (i.e., the focal depth of the mainshock; Fig. 6a; Table 1). Of these, two lobes were in the direction of both strikes, while the others were perpendicular. In detail, the mainshock (event 4) is within the positive zone induced by the largest foreshock (event 3) (Fig. 6a), indicating that the coseismic stress of the foreshock induced the mainshock. This remained valid when we considered the uncertainty of the location and the 3-D geometry in the vertical cross-section (Fig. 6b)

Fig. 5 Results of the relocation and focal mechanism analysis for the Goesan earthquakes. **a** Map view of the relocated 42 earthquakes (open circles) and retrieved three fault plane solutions. $S_{H\max}$ is the maximum horizontal stress indicated by a thicker solid grey line (Soh et al. 2018). Red circle indicates events constituting the main fault (Table 1). **b** Fault-plane view. The cross-section is indicated by a dashed grey line in (a). Dashed circle indicates the rupture area with r_0 of 0.20 km for the Mw 3.8 mainshock (event 4). A square having the same area as that of the circle with width of 0.35 km for event 4 is indicated with four corners. The square-shaped fault is used in the analysis of ΔCFS . **c** Fault-parallel view. Origins in (b) and (c) are the coordinates of the largest foreshock (event 3; Mw 3.3) in Table 1



411 and c). Most of the perturbed epicenters by bootstrap-
412 ping were included in the positive zone (Fig. 6b); the
413 perturbed depths did not enter the negative zone in the
414 cross-section (Fig. 6c). Similarly, Fig. 6d–f shows the
415 horizontal and vertical slices of the ΔCFS with the
416 perturbed locations of the aftershocks of the main fault
417 (Table 1). The aftershocks were located in the positive
418 zone in the vertical cross-section (Fig. 6f).

4 Discussion

4.1 Earthquakes following the static stress increase

We confirmed that the change in the coseismic static stress of the Mw 3.3 foreshock explained the occurrence of the mainshock (Fig. 6a). The occurrence of aftershocks was well understood based on the

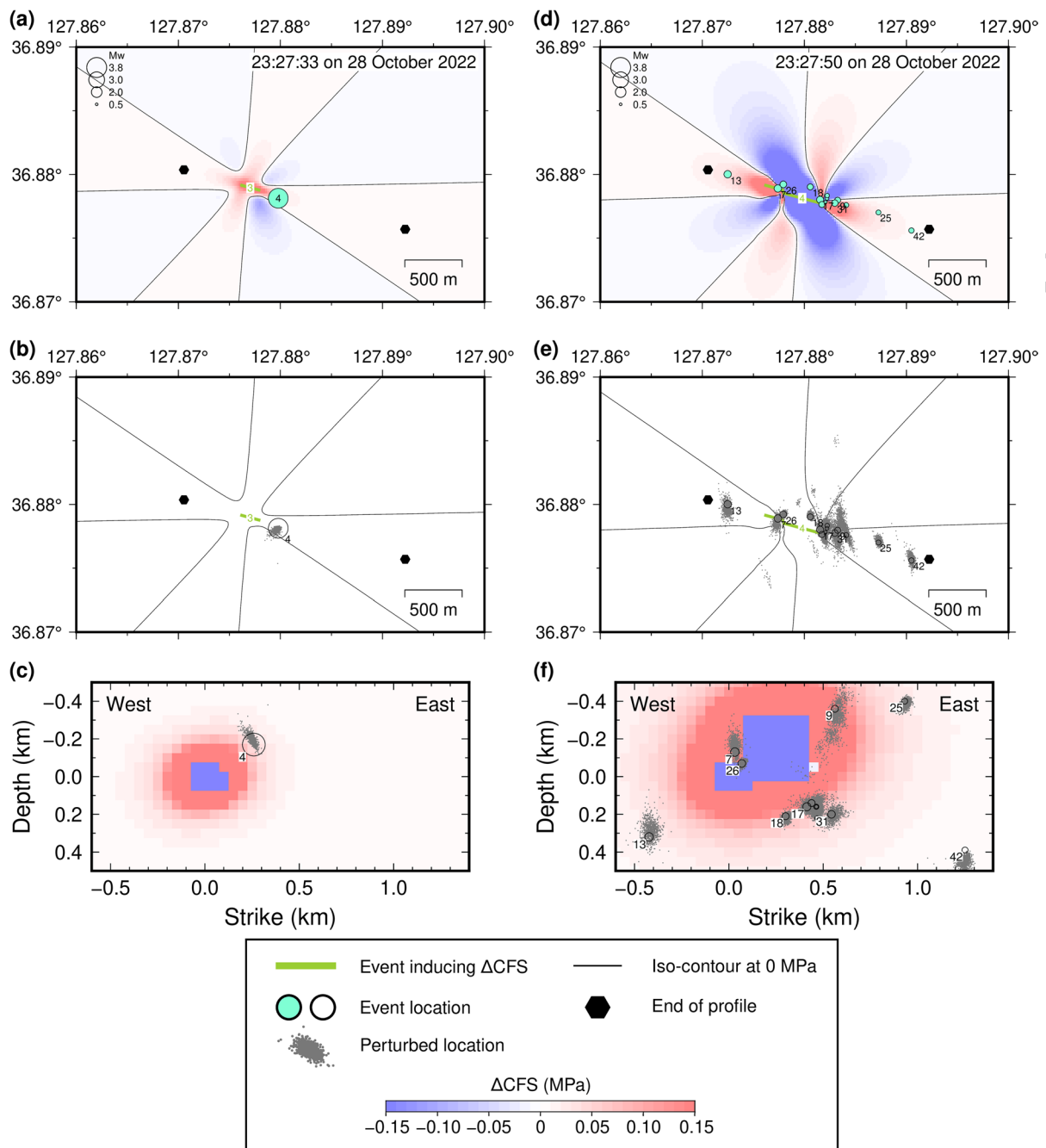


Fig. 6 Change in the Coulomb Failure Stress (ΔCFS) of the Mw 3.3 foreshock (event 3) and Mw 3.8 mainshock (event 4). The strike, dip, and rake of the receiver fault are 105° , 87° , and 13° , respectively. **a** ΔCFS of the Mw 3.3 foreshock. **b** Modified version from (a). Perturbed locations of the Mw 3.3 foreshock on the ΔCFS simplified by an iso-contour of 0 MPa. **c** Vertical cross-section of (a). **d** ΔCFS of the Mw 3.8 main-

shock added to the previous snapshot. The events within 100 m from the plane of the main fault, defined in Fig. 1, are only plotted. Time stamps in (a) and (d) indicate the origin times of the Mw 3.3 foreshock and Mw 3.8 mainshock, respectively (Table 1). **e** Modified version from (d), like (b), with the perturbed locations and the iso-contour of 0 MPa. **f** Vertical cross-section of (d)

cross-sectional view of the Δ CFS in the framework of the coseismic static stress (Fig. 6f). Events 7, 9, 17, 18, 26, and 31 were located near the edge of the rupture zone where the Δ CFS was highest (up to 0.15 MPa; Fig. 6f); although the upper limit near the rupture zone is sensitive to heterogeneous slip distribution, this was not determined in this study. Events 13, 25, and 42 were located relatively far from the rupture zone of the mainshock, extending the seismic zone to \sim 1.7 km horizontally and \sim 0.8 km vertically. Notably, this discussion presumes that the aftershocks had a similar focal mechanism as the mainshock.

4.2 The Mw 2.9 aftershock in the stress-shadow zone

The occurrence of the largest aftershock (event 30) in the negative Δ CFS zone is not simply explained in the Δ CFS (Fig. S7 in the supplementary materials). The applied stress tensor was the same as that for Fig. 6, however, the receiver fault was changed to the strike, dip, and rake of event 30. The epicenter of event 30 was at positive Δ CFS at the time of the largest foreshock (Fig. S7a in the supplementary materials); however, became negative at the time of the mainshock (Fig. S7b in the supplementary materials). Unlike other aftershocks in Fig. 6, event 30 does not conform to the 3-D geometry, mainly due to its depth of 12.89 km, a value close to the mainshock depth of 12.83 km (Table 1). However, we noticed that another study suggested that event 30 (event '25' in their article) was located in the positive Δ CFS zone (Kim et al. 2023). The crucial distinction is in the depth of event 30, which differs from that of event 4 in their study by 0.6 km (hypocentral) or -1.5 km

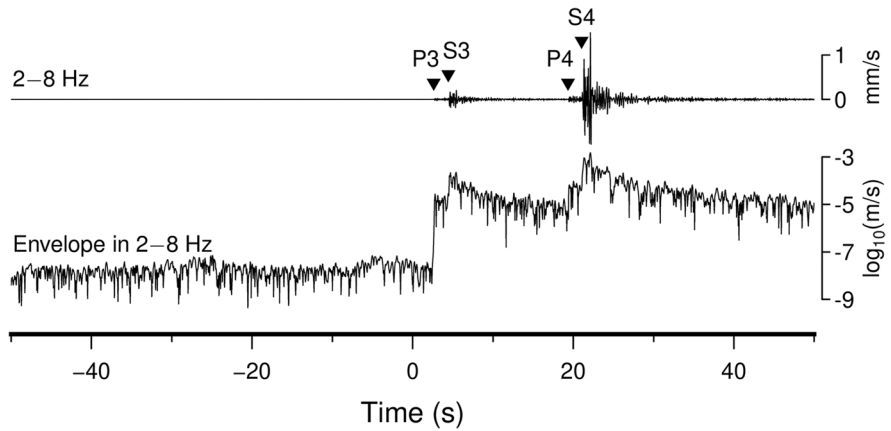
(centroid), while our results do not show this discrepancy. We also suggested alternative contributions to the occurrence of event 30: smaller events near event 30, such as event 16, could indicate a possible interaction between events 4 and 30 (Fig. 5). However, it is important to note that our understanding is limited, and further studies are needed to explore and validate these relationships. An oversimplified uniform rupture could be involved. Also, secondary mechanisms resulting from time-dependent changes in the frictional state can also affect the stress field (Dieterich 1994; Kilb et al. 2000; Freed 2005; Parsons 2005; Ree et al. 2021).

4.3 Limited implications from fore- and aftershocks

Foreshocks hold significant interest due to their potential role in triggering a mainshock; thus, it is crucial to comprehend the spatiotemporal features associated with their occurrence. Tape et al. (2018) found a notable observation that the high-frequency precursor in 2–8 Hz and the signal in the very low frequency band (0.02–0.05 Hz) are coincident within tens of seconds before the P arrival of the earthquake in central Alaska. However, we are unable to observe the high frequency precursor, following the same process as Tape et al. (2018). Traces filtered in the 2–8 Hz range and their log-scaled envelope in the top and bottom of Fig. 7 did not display any anomalous signal. The inspection for the wave in the very low frequency band is limited because of the short length of the window before the P arrival of the mainshock.

Waveform similarity can provide insights into the spatial feature of hypocenter distribution and

Fig. 7 Traces filtered in a high-frequency band. The station CHJ3's vertical trace is filtered in 2–8 Hz at the top. P3 and S3 indicate the P and S wave arrival times of the Mw 3.3 foreshock (event 3); P4 and S4 are for the Mw 3.8 mainshock (event 4). The trace at the bottom is a log-scaled envelope from the top image to show the possible existence of a small amplitude precursor, which is absent in this figure



be applied to cross-check the relocation outcomes (Schaff and Richards 2004; Kim et al. 2010, 2022; Son et al. 2015, 2020; Sheen 2021). We assessed waveform similarity by computing cross-correlation coefficients (CCs) for the high-pass-filtered at 1 Hz in a 0–6 s window from the time of origin to include P wave arrival time and S coda. We used waveforms recorded by the north–south component of station CHJ3, positioned with an azimuth of 93°, nearly parallel to the transverse direction of ten events (1–6, 14, 16, 17, and 30). The selected events encompassed the three of foreshocks (events 1–3), relatively large-magnitude events (3–6, 14, 16, 17, and 30).

The CCs were grouped into two clusters: C1 comprised events 1–4, and 30, while C2 comprised events 5, 6, 14, 16, and 17 (Fig. 8a). Although the CC of event 6 was low and events 5 and 6 had negative polarity, we included them in C2 due to shared monochromatic features observed in each spectrum, similar

to those present in the spectra of other events (14, 16, and 17) in C2 (Fig. 8b and c). The low CC of event 6 was due to a slightly low-frequency peak at 27 Hz (Fig. 8c). The monochromatic feature with an average peak at ~29 Hz, after the S wave arrival (Fig. 8b and c) could result from a trapped mode in a fault zone (Li et al. 1990; Ben-Zion 1998; Li and Vernon 2001; Ross and Ben-Zion 2015). However, the exceptions observed in events 17 and 30, along with their opposite positions toward each group, are contradictory to this possibility.

Instead, we observed the spatial coherence among hypocenters in C1 and C2, except for events 17 and 30 in C2 and C1, respectively (see also Fig. 5). Events 1–4, constituting the main fault, were included in C1, whereas events 5, 6, 14, and 16 from C2 were not associated with the main fault. It is also noteworthy that C1 includes the foreshock-to-mainshock sequence (4 of 5), while C2 predominantly comprises

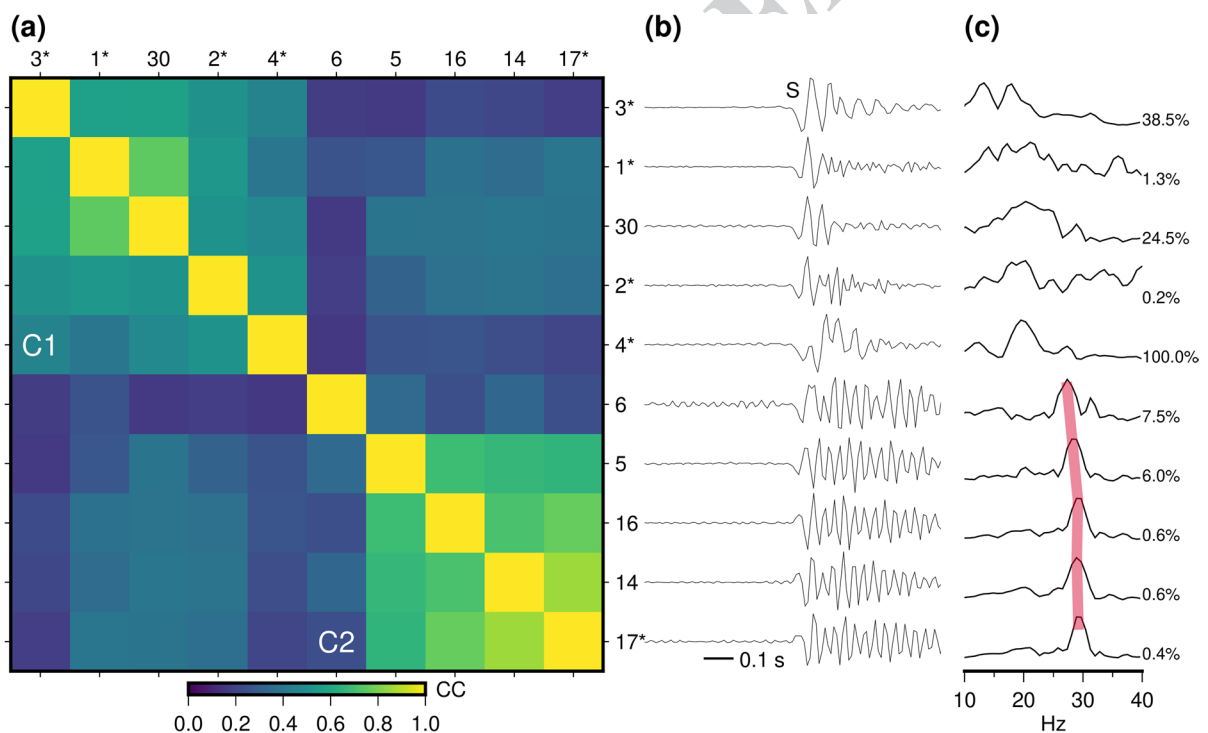


Fig. 8 Waveform similarity. **a** Cross-correlation (CC) matrix between the waveforms of station CHJ3 for the events labeled in Fig. 1. The events belonging to the main fault are marked by an asterisk. Cluster C1 comprises events 1–4, and 30, and C2 events 5, 6, 14, 16, and 17. **b** Transverse component aligned by the S arrival in a window from −0.5 to 0.5 s. The waveforms

are high-pass filtered at 1 Hz. The amplitude is normalized for visualization. **c** Spectra normalized in 10–40 Hz. The red line indicates peaks at ~29 Hz in the spectra of events 5, 6, 14, 16, and 17 having monochromatic phases after the S wave. The figure in percent in (c) indicates the relative scaling factor in terms of the peak amplitude of the mainshock

527 aftershocks. This observation may suggest the presence
 528 of structural or frictional heterogeneity at a local
 529 scale, indicating different faulting properties for each
 530 cluster within a relatively confined region around the
 531 main fault. The temporal distinction between foreshocks and aftershocks could further emphasize a
 532 possible mainshock-induced coseismic changes in the
 533 stress field of the confined region. This hypothesis
 534 needs additional waveform similarity analyses with
 535 more stations; however, we were not able to observe
 536 high-frequency waveform similarity at stations DKSA
 537 and CGAA, located relatively far from the epicenter
 538 to CHJ3, due to attenuated waveforms.

540 4.4 Coefficient A and stress drop ($\Delta\sigma$)

541 The A in Eq. (1) is described as $A = L/\beta$ where L is
 542 the fault's lateral width (Cesca et al. 2011). When we
 543 substituted A and β with 0.078 s and 3.5 km/s, respectively,
 544 L became 0.27 km, which was similar to the assumed square-shaped fault's width of 0.35 km in
 545 the calculation of the Δ CFS.

546 The $\Delta\sigma$ of 29 MPa for the mainshock (event 4)
 547 was larger than the average in the Korean Peninsula
 548 1–10 MPa for Mw larger than 3.5 of Rhee and Sheen
 549 (2016). Also, the $\Delta\sigma$ was slightly larger than those of
 550 the 2016 Mw 5.5 Gyeongju earthquake, 11 MPa of
 551 Chai et al. (2020) based on the code wave, 13 MPa
 552 of Son et al. (2018) based on the Snone method of S
 553 wave (Snone 1987), and 23 MPa of Uchide and Song
 554 (2018) based on the finite fault inversion with the
 555 empirical Green's function method. Uchide and Song
 556 (2018) reported that the local $\Delta\sigma$ on the fault was up
 557 to 62 MPa. Caution must be applied when comparing
 558 the absolute values of stress drops that were estimated
 559 using different methods (Shearer et al. 2019; Aber-
 560 crombie 2021; Calderoni and Abercrombie 2023).

562 5 Conclusions

563 The Mw 3.8 Goesan earthquake and its fore- and
 564 aftershocks represent a case with well-determined
 565 seismic properties owing to the dense national seis-
 566 mic networks and their geographical location in the
 567 central region of South Korea. Moreover, the rapid
 568 deployment of the temporary stations to provide
 569 azimuthal coverage within 10 km and one atop the
 570 mainshock epicenter improved the accuracy of the

571 foreshock, mainshock, and aftershock locations.
 572 Indeed, we shifted the hypocenters in terms of the
 573 coordinate of the largest aftershock that was deter-
 574 mined through full utilization of the aftershock array.

575 The focal mechanisms of the mainshock and its
 576 largest foreshock (Mw 3.3; event 3) and aftershock
 577 (Mw 2.9; event 30) indicate a left-lateral strike-slip,
 578 of which the P-axis corresponds with the maximum
 579 horizontal axis of the current tectonic stress. The
 580 west-northwest–east-southeast trending strikes of the
 581 faulting mechanisms agree with the spatial distribu-
 582 tion of the relocated hypocenters and the rupture
 583 directivity inferred from the azimuthal variation in
 584 corner frequency estimates obtained through source
 585 spectrum fitting. Based on the source spectrum fit-
 586 ting, we estimated the fault attributable to the main-
 587 shock. Its area of approximately 0.13 km² and the
 588 stress drop of 29 MPa.

589 The seismic properties identified the interaction
 590 between the mainshock and foreshock that preceded
 591 the mainshock by 17 s, as well as the development
 592 of most of the aftershock sequence. The mainshock
 593 occurred at the edge of the rupture zone, where the
 594 Δ CFS was positive. This indicates that the foreshock
 595 triggered the mainshock. Following the mainshock,
 596 the seismic zone propagated outside of the rupture
 597 zone. The cross-sectional view of the Δ CFS indicated
 598 that the aftershock distribution scattered horizontally
 599 and propagated downward from the rupture zone of
 600 the mainshock.

Acknowledgements We thank anonymous reviewers who
 601 gave helpful and thoughtful comments to improve the man-
 602 uscript. Our appreciation also goes to Kwan-Hee Yun, Jeong-
 603 Ung Woo, Sunyoung Park, and Won-Young Kim for con-
 604 structive discussion. We appreciate the Korea Meteorological
 605 Administration for providing seismic data. We would like to
 606 acknowledge efforts in the deployment of the aftershock moni-
 607 toring array for the participants, I.S. Lim, S.H. Lee, K.S. Kim,
 608 H.M. Cho, H.I. Cho, Y.W. Yun, T.W. Kim, D.H. Lee, Y.J.
 609 Seong, and T.S. Oh. Also, we thank the earthquake monitoring
 610 team who provided early information on the earthquake. We
 611 thank the providers of the software, Generic Mapping Tools
 612 (Wessel et al. 2019), Seismic Analysis Code (Goldstein and
 613 Snone 2005), Octave (<https://octave.org/>), Coulomb 3 (Lin and
 614 Stein 2004), and Inkscape (<https://inkscape.org/>).

Author contributions Hobin Lim: Conceptualization; Data
 616 curation; Software; Formal Analysis; Resources; Validation;
 617 Investigation; Visualization; Writing – original draft; Chang
 618 Soo Cho: Resources; Data curation; Software; Formal Analy-
 619 sis; Funding acquisition; Validation; Project administration;
 620 Writing – review & editing; Minkyung Son: Conceptualization;
 621

622 Formal Analysis; Writing – original draft; Writing – review &
623 editing.

624 **Funding** This study is supported by the Basic Research Project
625 of Korea Institute of Geoscience and Mineral Resources.

626 **Data availability** The waveform data used in this study,
627 including the cut and continuous data of the four temporary
628 stations, can be found at <https://doi.org/10.5281/zenodo.7690346>. Continuous waveform data from the Korea Institute of Geo-
629 science and Mineral Resources can be accessed at <https://data.kigam.re.kr/quake/> following approval. Continuous data from
630 the Korea Meteorological Administration can be accessed at
631 <https://necis.kma.go.kr/> following approval. The supplementary materials contain one table presenting the velocity model
632 used to locate the hypocenters.

633 **Code availability** Codes used in this study will be shared
634 upon reasonable request.

635 **Declarations**

636 **Competing interests** The authors declare no competing inter-
637 ests.

641 **References**

- 642 Abercrombie RE (2021) Resolution and uncertainties in esti-
643 mates of earthquake stress drop and energy release. Phil
644 Trans R Soc A 379:20200131. <https://doi.org/10.1098/rsta.2020.0131>
- 646 Bachura M, Fischer T (2019) Waveform cross-correlation for
647 differential time measurement: bias and limitations. Seismol
648 Res Lett 90:2005–2014. <https://doi.org/10.1785/0220190096>
- 650 Ben-Zion Y (1998) Properties of seismic fault zone waves and
651 their utility for imaging low-velocity structures. J Geophys
652 Res 103:12567–12585. <https://doi.org/10.1029/98JB00768>
- 654 Brune JN (1970) Tectonic stress and the spectra of seismic
655 shear waves from earthquakes. J Geophys Res 1896–
656 1977(75):4997–5009. <https://doi.org/10.1029/JB075i026p04997>
- 658 Brune JN (1971) Correction to “Tectonic stress and the spec-
659 tra, of seismic shear waves from earthquakes.” J Geophys
660 Res (1896–1977) 76:5002–5002. <https://doi.org/10.1029/JB076i020p05002>
- 662 Calderoni G, Abercrombie RE (2023) Investigating spectral
663 estimates of stress drop for small to moderate earthquakes
664 with heterogeneous slip distribution: examples from the
665 2016–2017 Amatrice earthquake sequence. JGR Solid
666 Earth 128:e2022JB025022. <https://doi.org/10.1029/2022JB025022>
- 668 Cesca S, Heimann S, Dahm T (2011) Rapid directivity detec-
669 tion by azimuthal amplitude spectra inversion. J Seismol
670 15:147–164. <https://doi.org/10.1007/s10950-010-9217-4>
- 671 Chai G, Yoo S-H, Rhie J, Kang T-S (2020) Stress-drop scal-
672 ing of the 2016 Gyeongju and 2017 Pohang earthquake
673 sequences using coda-based methods. Bull Seismol Soc
674 Am 110:2047–2057. <https://doi.org/10.1785/0120200132>
- 675 Dieterich J (1994) A constitutive law for rate of earthquake
676 production and its application to earthquake clustering.
677 J Geophys Res 99:2601–2618. <https://doi.org/10.1029/93JB02581>
- 678 Dreger DS (2003) 85.11 TDMT_INV: time domain seismic
679 moment tensor INVersion. In: International geophysics.
680 Elsevier, pp 1627
- 681 Eshelby JD (1957) The determination of the elastic field of an
682 ellipsoidal inclusion, and related problems. Proc R Soc
683 Lond A 241:376–396. <https://doi.org/10.1098/rspa.1957.0133>
- 684 Freed AM (2005) Earthquake triggering by static, dynamic,
685 and postseismic stress transfer. Annu Rev Earth Planet
686 Sci 33:335–367. <https://doi.org/10.1146/annurev.earth.33.092203.122505>
- 687 Goldstein P, Snook A (2005) SAC availability for the IRIS
688 community. Incorporated institutions for seismology data
689 management center electronic newsletter
- 690 Heidbach O, Rajabi M, Cui X et al (2018) The world stress
691 map database release 2016: crustal stress pattern across
692 scales. Tectonophysics 744:484–498. <https://doi.org/10.1016/j.tecto.2018.07.007>
- 693 Hong T-K, Lee J, Lee J et al (2023) Unravelling a midcrustal
694 seismogenic fault structure from a seismic sequence and
695 geophysical data: application to the 28 October 2022 M_L
696 4.1 Goesan earthquake in the central Korean Peninsula.
697 Geophys J Int 235:1117–1129. <https://doi.org/10.1093/gji/gjad292>
- 698 Kilb D, Gomberg J, Bodin P (2000) Triggering of earthquake
699 aftershocks by dynamic stresses. Nature 408:570–574.
700 <https://doi.org/10.1038/35046046>
- 701 Kim SJ, Kim SG (1983) A study on the crustal structure of
702 South Korea by using seismic waves. J Korean Inst Min-
703 ing Geol 16:51–61
- 704 Kim WY, Choi H, Noh M (2010) The 20 January 2007 Odae-
705 san, Korea, earthquake sequence: reactivation of a buried
706 strike-slip fault? Bull Seismol Soc Am 100:1120–1137.
707 <https://doi.org/10.1785/0120090069>
- 708 Kim S, Rhie J, Kim G (2011) Forward waveform modelling
709 procedure for 1-D crustal velocity structure and its appli-
710 cation to the southern Korean Peninsula. Geophys J Int
711 185:453–468. <https://doi.org/10.1111/j.1365-246X.2011.04949.x>
- 712 Kim WY, Park JY, Seo M-S et al (2022) The 14 December
713 2021 Mw 4.9 offshore Jeju island, Korea, earthquake:
714 seismological observation of an intraplate earthquake
715 provides insight into regional seismotectonics. Seism Rec
716 2:107–117. <https://doi.org/10.1785/0320220012>
- 717 Kim WY, Seo M, Park JY et al (2023) The 28 October 2022
718 Mw 3.8 Goesan earthquake sequence in Central Korea:
719 stress drop, aftershock triggering, and fault interaction.
720 Bull Seismol Soc Am 113:2416–2431. <https://doi.org/10.1785/0120230078>
- 721 Li Y-G, Vernon FL (2001) Characterization of the San Jacinto
722 fault zone near Anza, California, by fault zone trapped
723 waves. J Geophys Res 106:30671–30688. <https://doi.org/10.1029/2000JB000107>
- 724 4 Springer

- 732 Li Y-G, Leary P, Aki K, Malin P (1990) Seismic trapped
733 modes in the Oroville and San Andreas fault zones. *Science*
734 249:763–766. <https://doi.org/10.1126/science.249.4970.763>
- 735 Lin J, Stein RS (2004) Stress triggering in thrust and subduc-
736 tion earthquakes and stress interaction between the southern
737 San Andreas and nearby thrust and strike-slip faults:
738 stress triggering and fault interaction. *J Geophys Res*
739 109:B02303. <https://doi.org/10.1029/2003JB002607>
- 740 Madariaga R (1976) Dynamics of an expanding circular fault.
741 *Bull Seismol Soc Am* 66:639–666. <https://doi.org/10.1785/BSSA0660030639>
- 742 Minson SE, Dreger DS (2008) Stable inversions for complete
743 moment tensors. *Geophys J Int* 174:585–592. <https://doi.org/10.1111/j.1365-246X.2008.03797.x>
- 744 Myers SC, Johannesson G, Hanley W (2007) A Bayesian
745 hierarchical method for multiple-event seismic location:
746 Bayesian stochastic multiple-event location. *Geophys J
747 Int* 171:1049–1063. <https://doi.org/10.1111/j.1365-246X.2007.03555.x>
- 748 Park S, Ishii M (2015) Inversion for rupture properties based
749 upon 3-D directivity effect and application to deep earth-
750 quakes in the Sea of Okhotsk region. *Geophys J Int*
751 203:1011–1025. <https://doi.org/10.1093/gji/ggv352>
- 752 Park S-I (2005) Stratigraphy and geological structures of the
753 Ogcheon supergroup in the Jogok area, Goesan, Korea.
754 Seoul National University
- 755 Parsons T (2005) A hypothesis for delayed dynamic earthquake
756 triggering. *Geophys Res Lett* 32:L04302. <https://doi.org/10.1029/2004GL021811>
- 757 Ree J-H, Kim K-H, Lim H et al (2021) Fault reactivation and
758 propagation during the 2017 Pohang earthquake sequence.
759 *Geothermics* 92:102048. <https://doi.org/10.1016/j.geothermics.2021.102048>
- 760 Rhee H, Sheen D (2016) Lateral variation in the source param-
761 eters of earthquakes in the Korean Peninsula. *Bull Seismol
762 Soc Am* 106:2266–2274. <https://doi.org/10.1785/0120160085>
- 763 Ross ZE, Ben-Zion Y (2015) An algorithm for automated
764 identification of fault zone trapped waves. *Geophys J Int*
765 202:933–942. <https://doi.org/10.1093/gji/ggv197>
- 766 Schaff DP, Richards PG (2004) Lg-wave cross correlation
767 and double-difference location: application to the 1999
768 Xiuyan, China, sequence. *Bull Seismol Soc Am* 94:867–
769 879. <https://doi.org/10.1785/0120030136>
- 770 Shearer PM, Abercrombie RE, Trugman DT, Wang W (2019)
771 Comparing EGF methods for estimating corner frequency
772 and stress drop from *P* wave spectra. *JGR Solid Earth*
773 124:3966–3986. <https://doi.org/10.1029/2018JB016957>
- 774 Sheen D-H (2021) Analysis of the 2020 Haenam, Korea, earth-
775 quake sequence. *Geosci J* 25:33–42. <https://doi.org/10.1007/s12303-020-0038-3>
- 776 Sheen D-H, Seo KJ, Kim S et al (2023) A rapid and automatic
777 procedure for seismic analysis based on deep learning
778 and template matching: a case study on the M 4.1 Goesan
779 earthquake on October 29, 2022. *JGSK* 59:345–354.
780 <https://doi.org/10.14770/jgsk.2023.010>
- 781 Snee JA (1987) Stable determination of (Brune) stress drops.
782 *Bull Seismol Soc Am* 77:530–538. <https://doi.org/10.1785/BSSA0770020530>
- 783 Snee JA (2003) FOCEMC: FOCal MEchanism deter-
784 minations. In: Lee WHK, Kanamori H, Jennings PC,
785 Kisslinger C (eds) International handbook of earthquake
786 and engineering seismology (Part B). Academic Press,
787 San Diego, pp 1629–1630. [https://doi.org/10.1016/S0074-6142\(03\)80291-7](https://doi.org/10.1016/S0074-6142(03)80291-7)
- 788 Soh I, Chang C, Lee J et al (2018) Tectonic stress orienta-
789 tions and magnitudes, and friction of faults, deduced from
790 earthquake focal mechanism inversions over the Korean
791 Peninsula. *Geophys J Int* 213:1360–1373. <https://doi.org/10.1093/gji/ggy061>
- 792 Son M, Shin JS, Kim G, Cho CS (2015) Epicenter relocation of
793 two 2013 earthquake sequences in the Yellow Sea, Korea,
794 using travel-time double-differences and Lg-wave cross-
795 correlation. *Geosci J* 19:295–303. <https://doi.org/10.1007/s12303-014-0038-2>
- 796 Son M, Cho CS, Shin JS et al (2018) Spatiotemporal distribu-
797 tion of events during the first three months of the 2016
798 Gyeongju, Korea, earthquake sequence. *Bull Seismol Soc
799 Am* 108:210–217. <https://doi.org/10.1785/0120170107>
- 800 Son M, Cho CS, Lee HK et al (2020) Partitioned fault move-
801 ment and aftershock triggering: evidence for fault interac-
802 tions during the 2017 Mw 5.4 Pohang earthquake, South
803 Korea. *J Geophys Res Solid Earth* 125:e2020JB020005.
804 <https://doi.org/10.1029/2020JB020005>
- 805 Tape C, Holtkamp S, Silwal V et al (2018) Earthquake nuclea-
806 tion and fault slip complexity in the lower crust of central
807 Alaska. *Nat Geosci* 11:536–541. <https://doi.org/10.1038/s41561-018-0144-2>
- 808 Uchide T, Song SG (2018) Fault rupture model of the 2016
809 Gyeongju, South Korea, earthquake and its implication for
810 the underground fault system. *Geophys Res Lett* 45:2257–
811 2264. <https://doi.org/10.1002/2017GL076960>
- 812 Waldhauser F, Ellsworth WL (2000) A double-difference
813 earthquake location algorithm: method and application to
814 the northern Hayward Fault, California. *Bull Seismol Soc
815 Am* 90:1353–1368. <https://doi.org/10.1785/0120000006>
- 816 Wessel P, Luis JF, Uieda L et al (2019) The generic mapping
817 tools version 6. *Geochem Geophys Geosyst* 20:5556–
818 5564. <https://doi.org/10.1029/2019GC008515>
- 819
- 820
- 821
- 822
- 823
- 824
- 825
- 826
- 827
- 828
- 829
- 830
- 831
- 832
- 833
- 834
- 835
- 836
- 837
- 838
- 839
- 840
- Publisher's Note** Springer Nature remains neutral with regard to jurisdictional claims in published maps and institutional affiliations.
- Springer Nature or its licensor (e.g. a society or other partner) holds exclusive rights to this article under a publishing agreement with the author(s) or other rightsholder(s); author self-archiving of the accepted manuscript version of this article is solely governed by the terms of such publishing agreement and applicable law.

Journal:	10950
Article:	10201

Author Query Form

Please ensure you fill out your response to the queries raised below and return this form along with your corrections

Dear Author

During the process of typesetting your article, the following queries have arisen. Please check your typeset proof carefully against the queries listed below and mark the necessary changes either directly on the proof/online grid or in the 'Author's response' area provided below

Query	Details Required	Author's Response
AQ1	Please check if the affiliation is presented correctly.	
AQ2	Please check if all tables are presented correctly.	
AQ3	Please provide complete bibliographic details of reference [Dreger, 2003].	